INTERNATIONAL JOURNAL FOR NUMERICAL METHODS IN FLUIDS
*Int. J. Numer. Meth. Fluids* 2007; **53**:1801–1817
Published online 17 October 2006 in Wiley InterScience (www.interscience.wiley.com). DOI: 10.1002/fld.1379

# Numerical simulation of flapping-wing insect hovering flight at unsteady flow

Decan Zuo*,†, Songlin Peng‡, Wenyuan Chen§ and Weiping Zhang

*National Key Laboratory of Nano/Micro Fabrication Technology, Institute of Micro/Nanometer Science and Technology, Shanghai JiaoTong University, Key Laboratory for Thin Film and Micro Fabrication of Ministry of Education, Shanghai 200030, China*

SUMMARY

A computational fluid dynamics (CFD) analysis was conducted to study the unsteady aerodynamics of a virtual flying bumblebee during hovering flight. The integrated geometry of bumblebee was established to define the shape of a three-dimensional virtual bumblebee model with beating its wings, accurately mimicking the three-dimensional movements of wings during hovering flight. The kinematics data of wings documented from the measurement to the bumblebee in normal hovering flight aided by the high-speed video. The Navier–Stokes equations are solved numerically. The solution provides the flow and pressure fields, from which the aerodynamic forces and vorticity wake structure are obtained. Insights into the unsteady aerodynamic force generation process are gained from the force and flow-structure information. The CFD analysis has established an overall understanding of the viscous and unsteady flow around the virtual flying bumblebee and of the time course of instantaneous force production, which reveals that hovering flight is dominated by the unsteady aerodynamics of both the instantaneous dynamics and also the past history of the wing. A coherent leading-edge vortex with axial flow and the attached wingtip vortex and trailing edge vortex were detected. The leading edge vortex, wing tip vortex and trailing edge vortex, which caused by the pressure difference between the upper and the lower surface of wings. The axial flow, which include the spanwise flow and chordwise flow, is derived from the spanwise pressure gradient and chordwise pressure gradient, will stabilize the vortex and gives it a characteristic spiral conical shape. Copyright © 2006 John Wiley & Sons, Ltd.

Received 17 May 2006; Revised 18 August 2006; Accepted 22 August 2006

KEY WORDS: Navier–Stokes equations; unsteady three-dimensional incompressible flow; biological fluid mechanics

*Correspondence to: Decan Zuo, National Key Laboratory of Nano/Micro Fabrication Technology, Institute of Micro/Nanometer Science and Technology, Shanghai JiaoTong University, Key Laboratory for Thin Film and Micro Fabrication of Ministry of Education, Shanghai 200030, China.
†E-mail: zuodecan@sjtu.edu.cn
‡E-mail: pengsl@sjtu.edu.cn
§E-mail: chenwy@sjtu.edu.cn

Contract/grant sponsor: National Nature Foundation; contract/grant number: 60375033

## 1. INTRODUCTION

Flapping-wing Micro Aerial Vehicles (MAVs), with the promising characteristics of extraordinary flight capabilities, unmatched manoeuvreability, low-cost fabrication, has been a very active researching area both in civil and military applications [1–3]. Practical applications of flapping-wing MAV have been recognized for military missions such as battlefield reconnaissance, damage assessment, visual surveillance, biological or chemical agent sensing, and communications relay, and for civil missions such as search and rescue, border patrol, air sampling, and police surveillance. The size of the flapping-wing MAV is defined as the largest linear distance between any two points located on the vehicles. The target dimension of flapping-wing MAV is approximately 6 inch, and the development of an insect-size aircraft is expected in the near future.

In order to design the practical flapping-wing MAV, we must turn to the flapping-wing insect in nature, studying the aerodynamic mechanisms of them during hovering flight, forward flight, up-forward flight, down-forward flight and side flight, etc. Flapping-wing flight is one of the most interesting and challenging research subjects in the field of bionics and aeronautics. Flapping-wing flight style is employed by most flying creatures including birds, bats and insects. The range of Reynolds number of different flying creatures varies largely. A wide range of Reynolds number from approximately 10 for the smallest insects to approximately $10^4$ for large insects such as certain beetles, moths and butterflies, and up to approximately $10^5$ for most birds and bats are covered by the flying creatures [4]. The mechanism of flying creatures' flight is the focused question by most biologists and engineers. Flying creatures are different from conventional aircraft by beating their wings rapidly to change their attitude and flight velocity, performing manoeuvres with rapid accelerations and decelerations, and in quick plunging and pitching motions. So we need to study the aerodynamic mechanisms of the flying insects undergoing the three-dimensional unsteady and viscous flow around wings with a variable geometry.

Presently the researching about insects flight is mainly concentrated on two aspects, one is experimental observation on the kinematics of flying creatures and measurement of the aerodynamic force; the other is numerical simulation on the kinematics of flying insects. Both of the methods are intended to get the aerodynamic force, moment and the flying mechanisms of insects. In the experimental aspect, Maxworthy [5] succeeded in his pioneering experimental study in visualizing the near-field flow around a rigid three-dimensional model of the 'fling' motion and found a leading-edge vortex with span-wise flow. Cloupeau [6] measured instantaneous lift in tethered locusts, and concluded that unsteady mechanisms must generate extra lift forces. Wilkin [7] also succeeded in measuring the fluctuating lift forces on tethered locusts flying in a wind tunnel, finding that the peak lift was approximately twice the quasi-steady value. Wilkin [8] and Wilkin and Williams [9] produced further estimates of the flight forces of both locusts and moths, determining aerodynamic forces by subtracting estimates of the inertial forces from the measured forces. Dickinson *et al.* [10–12] conducted force measurements on flapping robotic fruit fly wings and showed that a large lift force was maintained during the translational phases of the up- and down-strokes and brief bursts of high lift occurred during stroke reversal when the wing was rotating. They explained the large lift force during the translational phases by the delayed-stall mechanism. Ellington *et al.* [13] performed flow-visualization studies on a hawkmoth *Manduca sexta* using a mechanical model of the hawkmoth wings. They discovered that the dynamic stall vortex on the wing did not shed during the translational motion of the wing in both the up- and down-strokes because it was stabilized by a strong spanwise flow. They suggested that this was a new mechanism of lift enhancement, which prolonged the benefit of the delayed stall for the entire stroke.



DOI: 10.1002/fld

With recent advances in computational fluid dynamics (CFD), many researchers have begun exploring numerical methods to explain the mechanisms of insects' flight. In the aspect of numerical simulation, one popular method that is available for computing the unsteady flow about arbitrary bodies is the potential flow panel method. Rayner [14] proposed a vortex theory of animal flight based on the wake being modelled as a series of vortex rings periodically shed into the wake, and elaborated the vortex theory of propulsion based on time dependent circulatory forces rather than estimated force coefficients. More recently, an extension of such a three-dimensional panel methods was developed by Vest [15], in which the motion of the body is prescribed and each wing is assumed to be rigid and rotating about a common axis. By following a time-stepping solution procedure, the shape of the trailing wake is determined. All vorticity is assumed to confine to the boundary layer on the surface of the body and in a thin vortex wake shed behind the body. Smith *et al.* [16] calculated the aerodynamic forces of flapping wings of a tethered moth by using an unsteady panel method. They were also describing the kinematics of a flapping wing relatively realistically and accounting for wing flexibility using the unsteady aerodynamic panel method. The results demonstrated good agreement with the experimental data obtained in the vertical force but not in the horizontal force. It is not clear whether the discrepancy was due to the lack of suction force or not. Liu *et al.* [17] by using a finite volume method, studied the unsteady aerodynamics of the flapping wing of a hovering hawkmoth. They analysed the mechanism of generation of the leading-edge vortex during one complete flapping cycle. The calculated vertical force was produced mainly during the down-stroke and the latter half of the up-stroke, with little force generated during pronation and supination. Sun and Tang [18, 19] simulated the flow around a model fruit fly wing using the method of computational fluid dynamics. They showed that in the case of advanced rotation the large lift peak at the beginning of the stroke by using simultaneously obtained forces and flow structures, which was due to the fast acceleration of the wing. They also found that the large lift peak near the end of the stroke was due to the fast pitching-up rotation of the wing. Wang [20] used a computational fluid dynamics method to study the aerodynamic force and vortex wake structure of an airfoil in dragonfly hovering mode. Time variation of the aerodynamic force in each flapping cycle and the vortex shedding process was obtained. In recent years, the wing kinematics data are available aided by the high-speed video, new methods such as digital particle image velocimetry (DPIV) to quantity flows, and powerful computers for simulation and analysis. With these methods, the study proceed with fewer simplifying assumptions to build more rigorous models of insect flight, it is this more detailed view of kinematics, forces and flows that has led to significant progress in our understanding of insect flight aerodynamics.

The present study intends to reproduce the flow around a flapping-wing insect as much as it could in details. In this paper, we conduct a computational fluid dynamics study on unsteady aerodynamic force generated by a virtual flying bumblebee during hovering fight. Unsteady aerodynamic forces and flow fields are achieved simultaneously by numerical solution of the Navier–Stokes equations.

## 2. NUMERICAL SCHEME

### *2.1. Coordinate systems definition and kinematics of wing*

The virtual flying insect considered in the present study is approximately the same as the natural bumblebee. Before the flow calculation method outlined below and the force discussion, three coordinate systems are introduced. They are described as follows: one is the inertial coordinate



DOI: 10.1002/fld

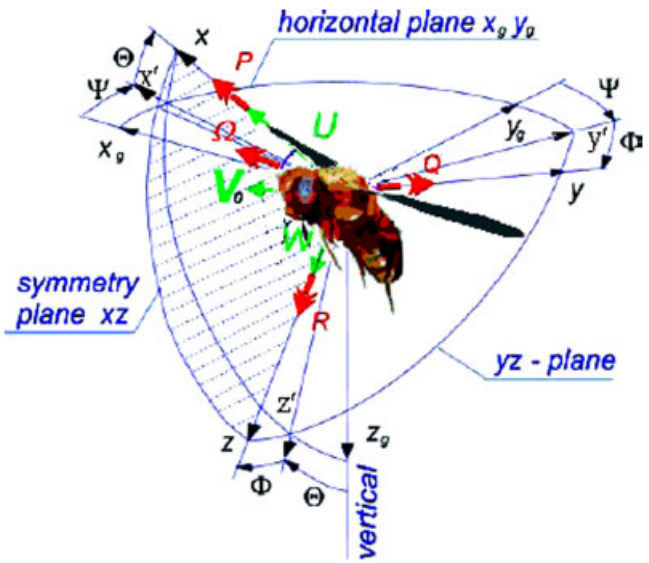


Figure 1. The coordinate systems of flying insects: $x_g, y_g, z_g$ is the inertial coordinate system; $x, y, z$ is the body-fixed coordinate system; $x', y', z'$ is the wing-fixed coordinate system.

system $ox_g y_g z_g$. The origin $O$ is at the centre of the flapping-wing insect. The $x_g$ and $y_g$ axes are in the horizontal plane with the $x_g$ axis positive fore, the $y_g$ axis positive larboard and the $z_g$ axis positive vertically down (see Figure 1). The second is the body-fixed coordinate system $oxyz$. It has the same origin as the inertial coordinate system, but it rotates following the insect body. The $x$-axis is parallel to the longitude of insect and positive fore, and the $y$-axis is on the positive larboard of insect body and $z$-axis perpendicular with the frame which formed by $x$-axis and $y$-axis (see Figure 1). The attitude of insect body can be defined by Euler angles $(\phi, \theta, \varphi)$, which describe the position between the inertial coordinate system and body-fixed coordinate system. The relationship between these two coordinate systems is given by

$$\begin{bmatrix} x_g \\ y_g \\ z_g \end{bmatrix} = \begin{bmatrix} c\varphi c\phi - s\varphi c\theta s\phi & c\varphi s\phi + s\varphi c\theta c\phi & s\varphi s\theta \\ -s\varphi c\phi - c\varphi c\theta s\phi & -s\varphi s\phi s\theta + c\varphi c\theta c\phi & c\varphi s\theta \\ s\theta s\phi & c\phi s\theta & c\theta \end{bmatrix} \begin{bmatrix} x \\ y \\ z \end{bmatrix} \tag{1}$$

The third coordinate system is wing-fixed coordinate system, which can be defined by $ox'y'z'$, where the origin of the wing-fixed coordinate system is same as the origin of body-fixed coordinate system, $x'$ is paralleled to the direction of wing-chord, $y'$ is paralleled to the direction of wingspan, $z'$ according to right-hand law (see Figure 2). The wing-fixed coordinate system is to describe the motion of wing. The kinematics of wing can be decomposed into three basic motions: (1) the flapping angle $\xi(t)$ of wings which moves around the $x$-axis of body-fixed coordinate system; (2) the lagging angle $\Psi(t)$ of wings which moves around the $z$-axis of body-fixed coordinate system; (3) the rotating angle $\zeta(t)$ of wings which moves around the $y$-axis of body-fixed coordinate system. The relationship between the body-fixed coordinate systems and wing-fixed coordinate



DOI: 10.1002/fld

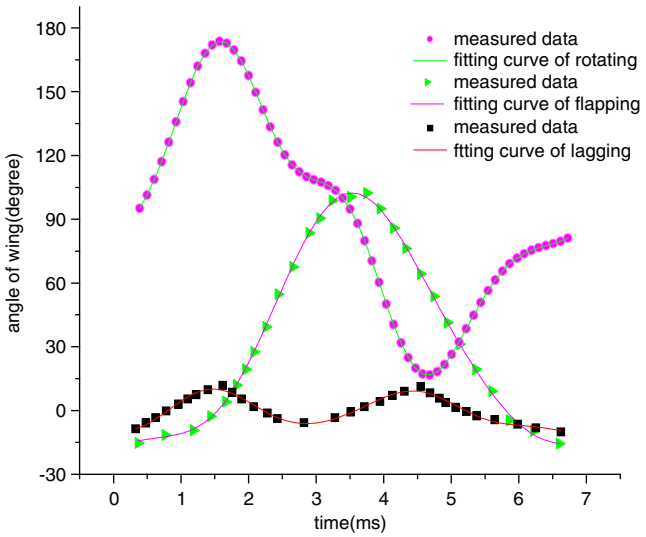


Figure 2. The time course of flapping, lagging and rotating angles of wing, the dot represent the measured data from the virtual flying bumblebee hovering flight, the line represent the fitting curve, which is described by four-phase Fourier series.

system is given by

$$\begin{bmatrix} x \\ y \\ z \end{bmatrix} = \begin{bmatrix} c\xi c\psi & c\xi s\psi s\zeta & c\xi s\psi c\zeta + s\xi s\zeta \\ s\xi c\psi & s\xi s\psi s\zeta & s\xi s\psi c\zeta - c\xi c\zeta \\ -s\psi & c\psi s\zeta & c\psi s\zeta \end{bmatrix} \begin{bmatrix} x' \\ y' \\ z' \end{bmatrix} \tag{2}$$

The integrated kinematics equations of wings may be expressed by Fourier equations, for the Fourier equation can describe any oscillating curve using a combination of sinusoidal functions with different coefficients and different periods. In this paper, we create kinematics equations of beating wing with the fewest number of parameters which accurately describe the wing motion using the limited raw data, which measured by Hao and Zeng [21]. The Fourier equation used is in the form

$$F(t) = a_0 + \sum_{n=1}^{n=m} (a_n \cos(n * k * t) + b_n \sin(n * k * t)) \tag{3}$$

where $F(t)$ is the amplitude in arbitrary units, $t$ is time, $a_o$, $a_n$ and $b_n$ are coefficients of Fourier equation, $k = (2 * f * c)/U$, where $f$ is the frequency of the flapping in Hertz, $c$ is the mean chord length in meters, $U$ is the reference velocity of wing in meters/second and $n$ goes from 1 to $m$. The larger the integer $m$ the more accurate the Fourier representation is due to the larger number of coefficients $a_n$ and $b_n$. In the present study, the reduced frequency $k = 0.926$, and we use the four phase Fourier series, which can accurately fit the measured kinematics data of flying insects. All the Fourier coefficients that describe the flapping, lagging and rotating motions of wing are illustrated by Table I.



DOI: 10.1002/fld

Table I. The coefficients of four-phase Fourier series which fit the measured data of virtual flying bumblebee.

| | $\xi(t)$ | $\Psi(t)$ | $\zeta(t)$ |
|---|---|---|---|
| $a_0$ | 31.40611 | −0.42556 | 92.82229 |
| $a_1$ | −57.31259 | −3.50094 | 4.81185 |
| $a_2$ | 11.60773 | −5.77778 | −4.38498 |
| $a_3$ | −1.18904 | −0.1215 | −11.76364 |
| $a_4$ | −0.13234 | 0.03593 | 3.35329 |
| $b_1$ | −11.83419 | 0.74006 | 59.56942 |
| $b_2$ | 3.37326 | 5.24608 | −7.55757 |
| $b_3$ | 1.75002 | −2.67426 | −8.97632 |
| $b_4$ | 0.37691 | −1.17588 | 0.13312 |

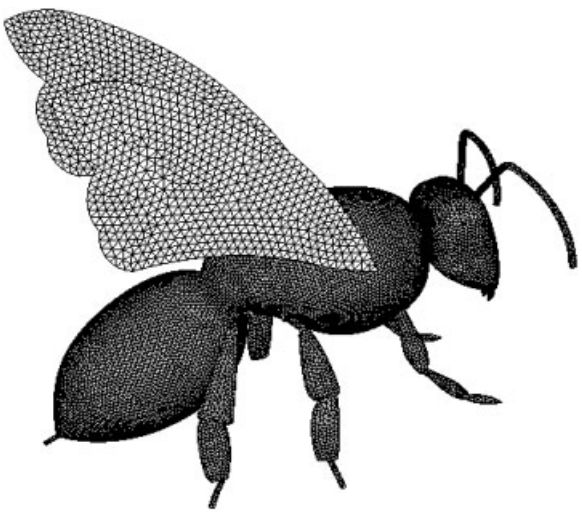

Figure 3. The insect model and the corresponding grids used in the computational fluid dynamics. Through resolving the N–S equation we can get the corresponding flowfield and the coefficients of aerodynamics force of flying insect.

### *2.2. Geometry and computational mesh*

The present study of virtual flying bumblebee is similar with the real bumblebees in nature, with the wing length 2.43 cm, wing area 1.85 $cm^2$, mean chord 0.76 cm, body length 2.53 cm, mass about 0.5 g, *Re* 2348, The wing length $R$ is $3.2c$, and radius of the second moment of wing area $r2$ is $0.58R$, where $c$ is the mean chord length.

The transient flow around the flapping-wing of a bumblebee has been simulated by CFD method. To facilitate resolution of the viscous flow at the leading edge, trailing edge and insect body as well as to accurately generate the modelling of insect, a tetrahedral grid topology is introduced (Figure 3). In this scheme, the whole physical domain is a sphere. A grid system with 1.15e5 nodes



DOI: 10.1002/fld

is generated around the wings and the body. Grids are clustered to the wing surface, in particular to the leading edge, the trailing edge and the insect body. To avoid unstable reflection of the solution at the open boundary, the distance was set far from the wing that is ten times of the length of insect. The configuration of the bumblebee is more complex, which include legs, body, head, antennas and wings. The analytic formulation for the wing motion is based on the measurement of Hao and Zeng. The fitting Fourier equations of flapping wing and the corresponding coefficients are described by Equation (3) and Table I.

The dynamic mesh model is used to simulate the flapping-wing motion of a realistic bumblebee applied as a time-varying boundary condition. The wing itself is idealized to be a rigid body with one fixed point at the joint of the wing, around which the wing is flapping, lagging and rotating. The movement vector of flapping-wing varies in different parts of the wings and direction over the duration of the flapping cycle. The bumblebee strokes its wings about at 150 Hz/s, so each cycle takes about 6.6 ms. To capture the detailed motion of bumblebee during the flight, a time-step of 0.05 ms is used, and dynamic remeshing is performed at every time step. The insect is assumed to be hovering flight in turbaned conditions, so a constant pressure field is applied to the inlet boundary upstream of the bumblebee in the model.

### *2.3. Flow solver*

In this study, we aimed to resolve the three-dimensional viscous flow around a flapping-wing insect (bumblebee). Since the Mach number of flapping-wing insect is very low during hovering flight, the relative motion between wing and the stream is very small, so the air is regarded as incompressible air. Unsteady three-dimensional flow around flapping-wing insect is numerically simulated. A resolution to the incompressible Navier–Stokes equations is the key to understanding such highly unsteady fluid mechanisms. We describe computational system based on the method of three-dimensional Navier–Stokes equation that can be directly applied to realistic biological problems. The three-dimensional incompressible unsteady Navier–Stokes equations in the conservative form of momentum and mass are nondimensionalized in the body-fixed coordinate system (see Figure 1), written in an integral form as

$$\frac{\mathrm{d}}{\mathrm{d}t}\int_V \rho\phi\,\mathrm{d}V + \int_{\partial V} \rho\phi(\mathbf{u}-\mathbf{u}_g)\cdot\mathrm{d}\mathbf{A} - \int_{\partial V} \Gamma\nabla\phi\cdot\mathrm{d}\mathbf{A} - \int_V S_\phi\,\mathrm{d}V = 0 \tag{4}$$

where $\rho$ is the fluid density; $\mathbf{u}$ is the flow velocity vector; $\mathbf{u}_g$ is the grid velocity of the moving mesh; $\Gamma$ is the diffusion coefficient; $S_\phi$ is the source term of $\phi$. Here $\partial V$ is used to represent the boundary of the control volume $V$. The time derivative term in Equation (4) using a first-order backward difference formula, can be written as

$$\frac{\mathrm{d}}{\mathrm{d}t}\int_V \rho\phi\,\mathrm{d}V = \frac{(\rho\phi V)^{n+1} - (\rho\phi V)^n}{\Delta t} \tag{5}$$

where $n$ and $n+1$ denote the respective quantity at the current and next time level. The $(n+1)$th time level volume $V^{n+1}$ is computed from

$$V^{n+1} = V^n + \frac{\mathrm{d}V}{\mathrm{d}t}\Delta t \tag{6}$$



DOI: 10.1002/fld

where $\mathrm{d}V/\mathrm{d}t$ is the volume time derivative of the control volume. In order to satisfy the grid conservation law, the volume time derivative of the control volume is computed from

$$\frac{\mathrm{d}V}{\mathrm{d}t} = \int_{\partial V} \mathbf{u}_g \cdot \mathrm{d}\mathbf{A} = \sum_{j}^{n_f} \mathbf{u}_{g,j} \cdot \mathbf{A}_j \tag{7}$$

where $n_f$ is the number of faces on the control volume and $\mathbf{A}_j$ is the $j$ face area vector. The dot product $\mathbf{u}_{g,j} \cdot \mathbf{A}_j$ on each control volume face is calculated from

$$\mathbf{u}_{g,j} \cdot \mathbf{A}_j = \frac{\delta V_j}{\Delta t} \tag{8}$$

where $\delta V_j$ is the volume swept out by the control volume face $j$ over the time step $\Delta t$.

The simulation used commercially available CFD software (Fluent). The governing equations are discretized using the finite volume method (FVM) and are solved in a time-marching manner using the pseudo-compressibility technique. A third-upwind differencing scheme is used to compute the convective term in an ultimate conservative difference scheme, the time-dependent solution to the governing equations is realized by introducing an inner iteration to allow the divergence of velocity to vanish at each physical time step, and the time derivatives in the momentum equations are differenced using a first-order, two-point, backward-difference implicit formula. A moving grid system is introduced to make grids fit the moving and deforming wing at each physical time step, and therefore to ensure sufficient grid density in resolving the viscous and unsteady flows around the wing surface.

### *2.4. Initialization and boundary conditions*

The process of virtual flying bumblebee during hovering flight in nature is a complex biological system, The three-dimensional effect of flapping-wing insect during flight exists, and the stream influence between the wings and body also exist, so the flow field of flapping-wing insect is in fact a three-dimensional flow field, adopting the two-dimensional flow field is not comprehensive. So the three-dimensional flow field was adopted in this numerical simulation. In fact, the wing surface of insect is distributed seta, squama and other apparatus, these structures will destroy the boundary layer of wing, and the deformed wing during flight also influence the flow field, but are all negligible in this study. The wing is regarded as no-slip and rigid body.

At the beginning of numerical simulation, supposing the insect is still, during hovering flight, it meets the initial flow field condition

$$\mathbf{V}_{t=0} = \mathbf{V}_\infty = u_\infty \mathbf{i} + v_\infty \mathbf{j} + w_\infty \mathbf{k} \tag{9}$$

where $\mathbf{V}_\infty$ is the inflow velocity of far-field. Since the insect is at the hovering flight, the velocity is zero. When insect is in free flight, the velocity of inflow is the reversed velocity of insect, where $\mathbf{i}, \mathbf{j}, \mathbf{k}$ are the unit vector of coordinate system.

On the surface of wing, where it meets the no-slip wall condition

$$\mathbf{V}_C = \mathbf{V}_{\text{wing}} \tag{10}$$



DOI: 10.1002/fld

where $C$ is the boundary curve of wing surface, $\mathbf{V}_{\text{wing}}$ is the instant velocity of the boundary of wing.

In the far-field boundary, the flow field meets

$$\mathbf{V}_{(x,y,z)\to\infty} = \mathbf{V}_{\infty} \tag{11}$$

## 3. COMPUTED RESULTS AND ANALYSIS

### *3.1. The unsteady vortex comparison between the numerical and experimental results*

To establish the validity of the bumblebee model in simulating the aerodynamics during hovering flight, a comparison between the computed flows and the experimental results of Van den Berg and Ellington [22] is presented. Van den Berg and Ellington used high-speed video to record the flow around the flapper with smoke released from the leading edge. The visualized flows were given at five span-wise cross sections at distances of $0.25R$, $0.5R$, $0.63R$, $0.75R$ and $0.87R$ from the base, respectively. The comparison of the flowfield between the numerical and experimental results is shown in Figure 4. The flows at three different positional angles are recorded during the down-stroke. For comparison, the computed flows are visualized at the corresponding three positions and the instantaneous velocity vector fields are plotted in side views relative to the stroke plane. The coloured velocity indicates the different velocities along the wing surface. There is good qualitative agreement between the numerical simulation results and the experimental results. The numerical simulation results also show that axial flow at the core of the leading-edge vortex during the middle and late down-stroke, giving the vortex a spiral conical shape. Also, the negative pressure region over the wing surface near the leading edge matches quite well with the location of the measured cores of the leading-edge vortices. Additionally, a span-wise flow can be seen during the numerical simulation. The shed vortex from the early half of the down-stroke can still be seen above the wing, which is in good agreement with the smoke visualized flow in Figure 4. A strong wing tip vortex with large velocity magnitudes is detected at the position where the leading-edge vortex breaks down and is shed from the wing tip. The measured time course of instantaneous forces to balance the bumblebee weight is analysed in the latter parts of this paper, and the calculated results have the good agreement with the natural phenomena.

### *3.2. The analysis of flowfield during down-stroke and up-stroke*

During the period of the down-stroke, as illustrated in Figure 5, the wings were flapping down accompanied with the rotating and lagging motion. Thus, the motion of the flapping wing is the combination of the three different motions along the axes. The pressure field and streamline of flapping-wing insect are illustrated by Figures 5 and 7. From the figures we can see that at the beginning of down-stroke, a coherent leading-edge vortex stretches from the base to the wing tip along the leading edge. The leading-edge vortex is from the lower surface to upper surface. When the wing moves to a horizontal position, the leading edge vortex become a large, spiralling vortex with strong axial flow on the upper wing surface and a new negative vorticity has formed around the leading edge and upper surface of the wing, and a new layer of positive vorticity has formed below the lower surface of the wing extending beyond its trailing edge. The negative pressure on the wing surface will contribute to the generation of lift force. With the increasing of up-stroke, the



DOI: 10.1002/fld

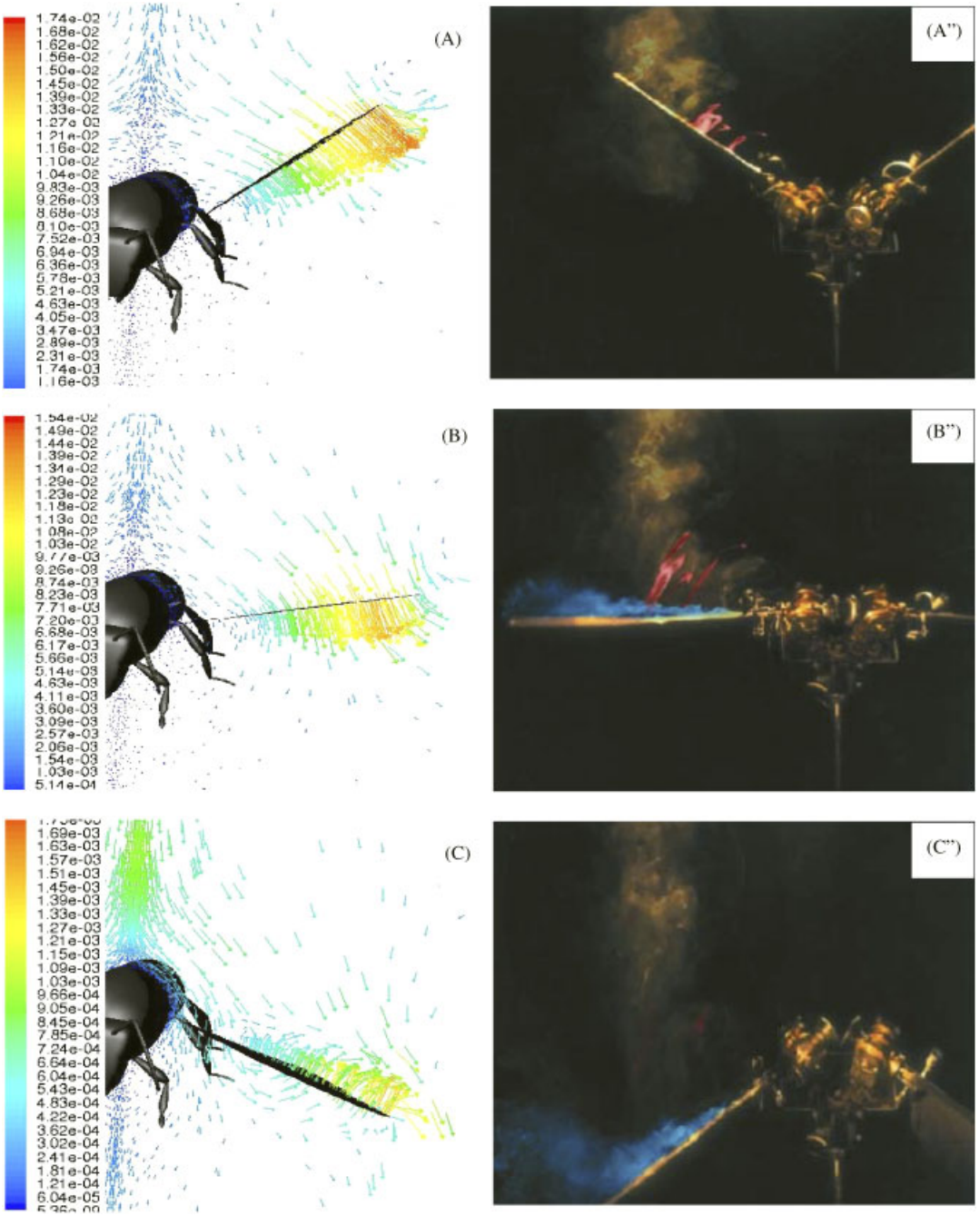


Figure 4. The vectors of air velocity is plotted from A to C at three different positional angles; Smoke-visualized flows conducted by Berg and Ellington at the same position during down-stroke. The smoke is released from the leading edge and the corresponding vortex is observed on the upper surface of wing.



DOI: 10.1002/fld

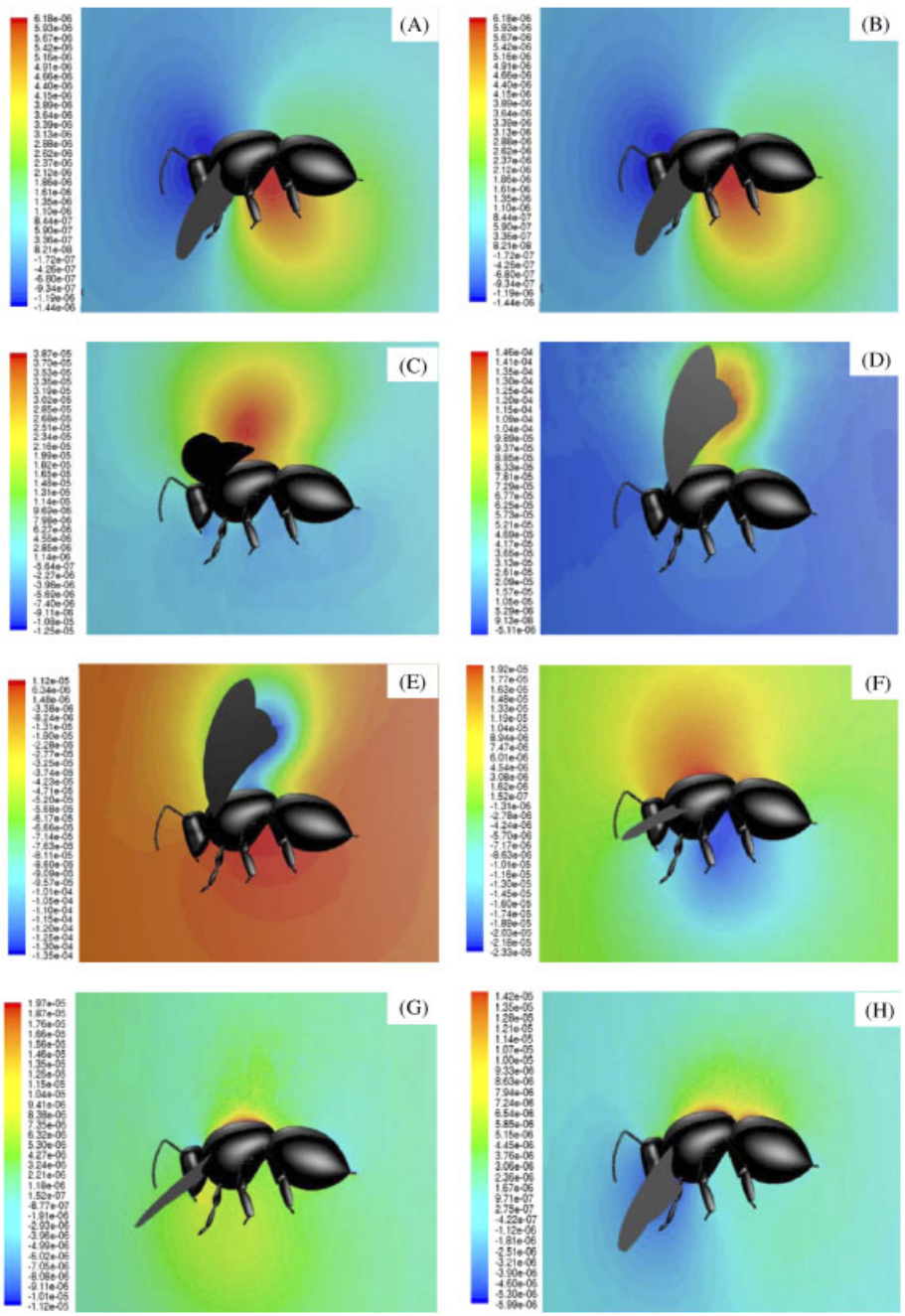


Figure 5. Pressure plots of flapping-wing insect from side view during up- and down-stroke (from left to right, from up to down). Red denotes higher pressure, and blue denotes lower pressure. The changing pressure field around flapping-wing insect is achieved, which can be explaining the lift generation mechanism of flying insect.



DOI: 10.1002/fld

leading edge vortex and trailing edge vortex break down slowly. The breakdown and separation of the leading edge vortex into the tip vortex is because of the instability of the flow with the reverse pressure gradient combined with the onset of wing deceleration after the middle of the down-stroke. The leading edge vortex does not show a significant change from the base to the wing tip position. At the end of the down-stroke, a new leading-edge vortex is created between the wing tip and the broken down position. The new leading-edge vortex shows a spiral axial flow and directed towards the base, which distributed along the leading edge and connects to the original leading-edge vortex. The axial flow is probably created by the reversed pressure gradient originally generated by the tip vortex. The new leading-edge vortex is strongly affected by the tip vortex and is relatively unstable. During the down-stroke, the new leading-edge vortex begins to be pushed off the leading edge because of the deceleration of the wing, and the breakdown point of the original leading-edge vortex moves towards the wing tip, and the generated lift decrease steeply.

During the up-stroke, a very small leading-edge vortex appears along the leading edge of wing. It is not separated, like a tip vortex. With the increasing of the angle of up-stroke, the leading edge vortex growing slowly, and the vortex extends from the base to the wingtip. The separated starting vortex cannot be observed during the early up-stroke. The leading-edge vortex is limited to a narrow region close to the wing tip and affects force generation at this moment, and the pressure of upper wing surface is larger than the lower wing surface, which caused the generated lift begin to decrease. While the wing reaches the middle position, the vortex from the wing tip to the base is decreasing. The vortex is tightly attached to the leading edge but merely leads to a very small negative pressure region at the wing tip. The flow follows both the upper and lower surfaces smoothly. The axial flow at the core of the vortex is not very distinguished, and the leading edge vortex and trailing edge vortex increase slowly. After the middle of the up-stroke, the leading-edge vortex grows rapidly, and at the same time, there exist the upper surface vortex and lower surface vortex slowly, which will contribute to the rotating of wing. With the angle of up-stroke increasing, the vortex breaks down slowly, but there is no significant shedding of the tip vortex, which is quite different from the down-stroke, and the generated lift decrease steeply.

### *3.3. The generated aerodynamic force*

Once the Navier–Stokes equations are numerically solved, the fluid velocity components and pressure at discretized grid points for each time step are available. The aerodynamic forces acting on the wing are calculated from the pressure and the viscous stress on the wing surface. In the calculation, the wings start the flapping motion in still air and the calculation is ended when periodicity reached the time of approximately 5–10 periods, which the aerodynamic forces and flow structure is approximately produced steadily. The aerodynamic forces is calculated in flapping plane, respectively, are lift and drag, can be illustrated by Figure 6.

Figure 6 shows the time course of lift and drag coefficient during flapping flight, computed by the discretized grid systems. From the figure, it can be seen that there are two large lift coefficient peaks in one cycle, one is in the first half of the cycle, while the flapping-wing is in its up-stroke, and the other in the second half of the cycle, while the flapping-wing is in its down-stroke, and the second lift peak is obviously bigger than the first lift peak. It should be noted that by having two large lift coefficient peaks alternatively in the first and second halves of a cycle, and the flapping cycle is very short, so the flight would be smoother.



DOI: 10.1002/fld

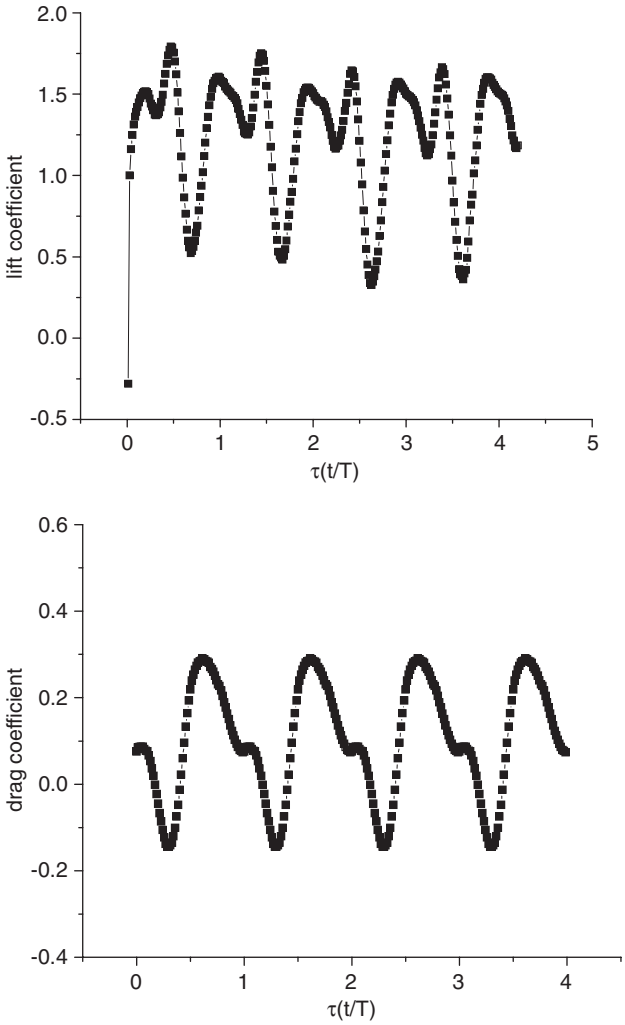


Figure 6. Time course of lift and drag coefficient during up- and down-stroke of flapping-wing insect. The $x$-axis is denotes no-dimensional time, and the $y$-axis denotes lift and drag coefficient.

To assess whether the lift force generated from the present numerical computation is capable of supporting the hovering bumblebee flight or not, the force balance is investigated during one complete flapping cycle, and a mean lift coefficient of 1.25 is obtained. Note that the force coefficients are non-dimensional by normalization to the maximum velocity during one flapping cycle. Given the reference velocity $U = 0.58R\varphi n = 4.45\,\mathrm{m\,s^{-1}}$ and the surface area $S = 1.85\,\mathrm{cm}^2$ of a real bumblebee wing, the lift coefficient $F_\mathrm{L}$ is equal to

$$F_\mathrm{L} = 0.5 C_\mathrm{L} \rho U^2 S \tag{12}$$



DOI: 10.1002/fld

where 1.225 $\mathrm{kg\,m^{-3}}$ is taken as the density of air $\rho$. The total lift force of wing is therefore calculated and the result is 2.8 mN. The mean force required per wing is half the weight of the bumblebee (mass about 0.5 g) or approximately 2.5 mN. Hence, the calculated mean force in a complete flapping cycle is about 1.12 time of the requirement to support the weight of the bumblebee.

### *3.4. The unsteady vortex and axial flow*

Most studies of insect flight have assumed either quasi-steady aerodynamics or some inviscid formulation, such as the doublet-lattice method for numerical simulation. However, the generated lift utilizing these methods cannot support the insect weight, no more than the manoeuvreability flight. In fact, during the process of insect hovering flight, the unsteady vortex bubble caused by flow separation from the sharp leading edge and the trailing edge contribute to the high lift generation, and the wing tip vortex (WTV) also contribute to the high lift generation. The axial flow, which includes the span-wise flow and chord-wise flow, will stabilize the leading edge vortex and trailing edge vortex. As shown in Figure 7, a leading-edge vortex (LEV), trailing-edge vortex (TEV) and wingtip vortex are observed. The pressure gradient of the unsteady vortex is probably the reason that caused axial flow. The pressure difference between the upper wing surface and the lower wing surface is the possible reason that caused the unsteady vortex along the wing edge. The velocities of different parts of flapping wings vary largely during the up-stroke and down-stroke, which would be the reason that the axial flow exist and the reason that the different vortex production along the wing edge. Since the velocity of wing tip is larger than other parts of wings, the wing tip vortex is greatly distinguished with the leading-edge vortex and trailing-edge vortex. The unsteady vortex does not breakdown due to the flow is fully three-dimensional vortex. The span-wise flow contribute to stabilize the unsteady vortex, and the span-wise flow convects the vorticity out toward the wing tip, where it joins with the wing tip vortex and prevents the leading edge vortex from growing so large that breakdown occurs. Under the low Reynolds number during insect flight, the pressure difference between the leading edge vortex and the trailing edge vortex caused the chord-wise flow, which also contributes to the stabilization of the unsteady vortex. In Figure 7, we can observe the span-wise flow and the chord-wise flow, but they are not very distinguished. The steep span-wise pressure gradient is due to the different velocities of the wing surfaces. The produced span-wise flow can concentrate the leading edge vortex, preventing it from accumulating into a large vortex that would be unstable. During the down-stroke, an intense spiral-shaped leading edge vortex and trailing-edge vortex with strong span-wise flow and chord-wise flow forms and a low-pressure region to grow on the upper wing surface is caused, and the high lift is generated at the same time. At the middle of down-stroke, there exist the upper surface vortex (USV) on the wing surface, which close to the trailing edge of wing, and the lower surface vortex (LSV) under the wing surface, which is close to the leading edge of wing. The appearance of upper surface vortex and lower surface vortex will contribute to the rotating of wing. During the latter down-stroke, the span-wise flow change its direction, which runs from the wing-tip toward the wing-base due to the pressure difference between the base and the tip vortex, and the wing base vortex (WBV) is observed at the base of wing. During the transition from the down-stroke to the upstroke, the leading-edge vortex and the trailing-edge vortex merge into a single hook-shaped vortex that quickly becomes deformed and then sheds from the trailing edge. During the upstroke, the unsteady flow is quite small, between the upper and lower wing surfaces, the pressure gradient is not very distinguished, and the corresponding lift is very small. At the latter upstroke, another



DOI: 10.1002/fld

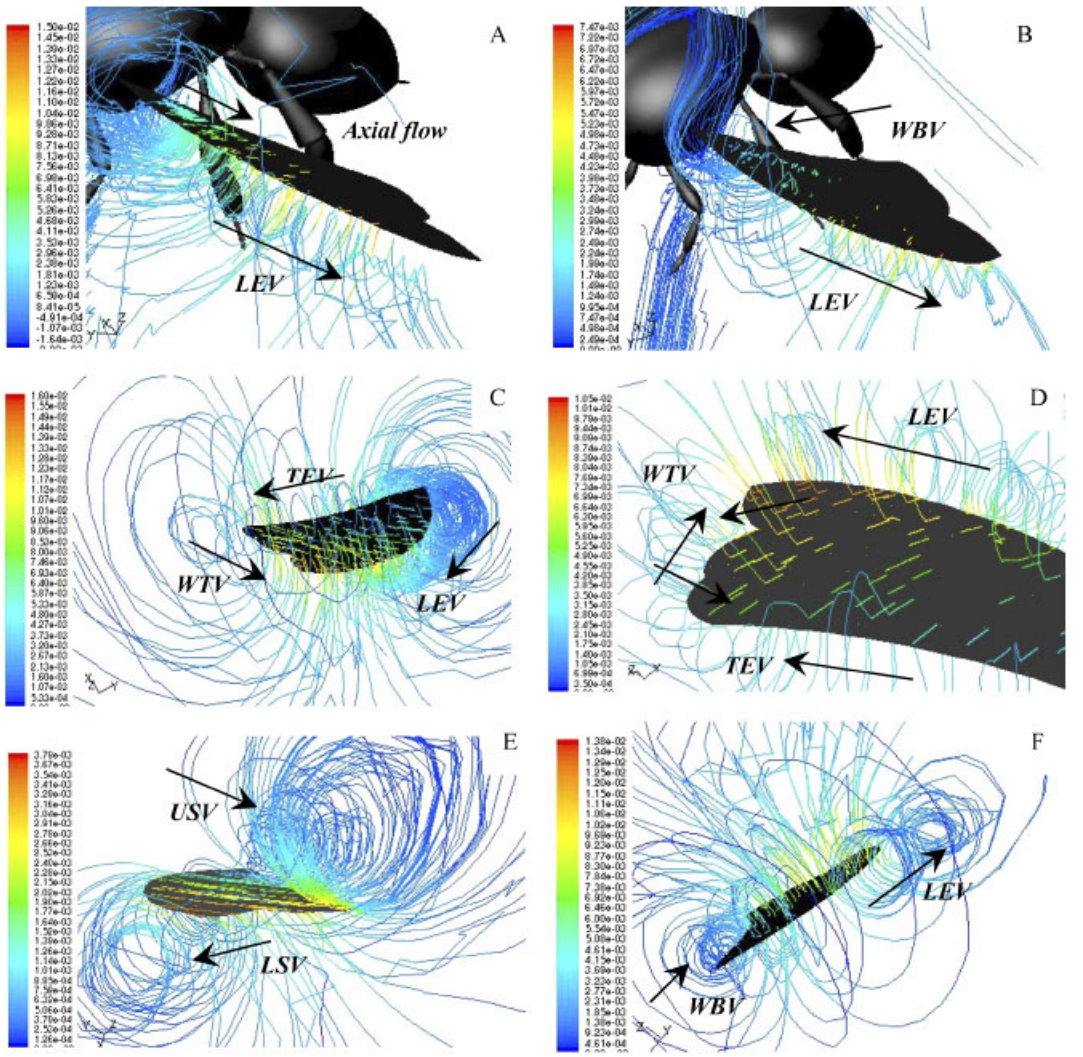


Figure 7. CFD-visualized flows with instantaneous streamlines are plotted from A to F during up- and down-stroke of flapping-wing insect. When the wing moving is accompanied with flapping, lagging and rotating, such vortex like leading-edge vortex, trailing-edge vortex, wing-base vortex, upper surface vortex, lower surface vortex and axial flow are observed. These especial vortex and axial flow will contribute to the high lift generation.

leading edge vortex grows on the underside of the wing and causes decreasing lift force. At the transition between the up-stroke to down-stroke, a small trailing edge vortex on the lower surface and a shear layer vortex on the upper surface are produced. The leading-edge vortex and span-wise flow have also been discovered by Liu *et al.* [17], which conducted a CFD study employing a model-wing of the hawkmoth, and the experimental research was carried out by van den Berg and Ellington [22, 23].



DOI: 10.1002/fld

## 4. CONCLUSION

The above work demonstrates the feasibility of numerical simulation based on a time-accurate solution of the Navier–Stokes equations of unsteady, viscous flow field structure around a flapping-wing insect with the flapping, lagging and rotating motion in the three-dimensional space. The unsteady aerodynamics of a real flapping-wing insect was successful modelled and the accurately prediction of the existence and timing of occurrence of the complex vortex structure was established in this paper. The present results also point out the importance of the existence of a very sophisticated lift-enhancement mechanism due to the spiral leading-edge vortex at low Reynolds number appropriate to insect flight. This paper has also studied the time course of instantaneous force production and the calculated lift can support the weight of insect. In the numerical simulation the flapping-wing is not regarded as an elastic deformation wing for their limited deformed shape during the up-stroke and down-stroke. In summary, the simulation has shown that with the introduction of dynamic mesh model, it is possible to simulate the three-dimensional flow around flapping-wing insect to better understand the unsteady aerodynamics of insects, and contribute to the development of flapping-wing MAV.

ACKNOWLEDGEMENTS

This research is supported by the National Nature Foundation (60375033) and the authors would like to thank all other members of research team for their contributions to this simulation project. Special thanks are owed to Dr S. Y. Yang and Professor H. Y. Yang for their great support and contributions in constructing the insect geometry and the discussion of flying mechanism.

REFERENCES

1. Azuma A, Masato O, Kunio Y. Aerodynamic characteristics of wings at low Reynolds Numbers. Fixed and flapping wings aerodynamics for micro air vehicle applications. In *Progress in Astro. & Aero.*, vol. 195, Mueller TJ (ed.), 2001; 341–398.
2. Fearing RS, Chiang KH, Dichinson MH. Wing transmission for a micromechanical flying insect. *Proceedings of the 2000 IEEE*, *International Conference on Robotics & Automation*, San Francisco, CA, April 2000; 1509–1516.
3. Ho S, Nassef H, Pornsinsirirak N. Unsteady serodynamics and flow control for flapping wing flyers. *Progress in Aerospace Science* 2003; (39):635–681.
4. Creenwalt CH. The flight of birds. *Transactions of the American Philosophical Society* 1975; **65**:1–67.
5. Maxworthy T. Experiments on the Weis–Fogh mechanism of lift generation by insects in hovering flight. Part 1. Dynamics of the 'flying'. *Journal of Fluid Mechanics* 1979; **93**:47–63.
6. Cloupeau M. Direct measurements of instantaneous lift in desert locust; comparison with Jensen's experiments on detached wings. *Journal of Experimental Biology* 1979; **180**:1–15.
7. Wilkin PJ. The instantaneous force on a desert locust, Schistocerca gregaria (Orthoptera: Acrididae), flying in a wind tunnel. *Journal of the Kansas Entomological Society* 1990; **63**:316–328.
8. Wilkin PJ. Muscle performance in hovering hummingbirds. *Journal of Experimental Biology* 1993; **178**:39–57.
9. Wilkin PJ, Williams HM. Comparison of the aerodynamic forces on a flying sphingid moth with those predicted by quasi-steady theory. *Physiological Zoology* 1993; **66**:1015–1044.
10. Dickinson MH, Lehman FO, Sane SP. Wing rotation and the aerodynamic basis of insect flight. *Science* 1999; **284**:1954–1960.
11. Sane SP, Dickinson MH. The control of flight force by a flapping wing: lift and drag production. *Journal of Experimental Biology* 2001; **204**:2607–2626.
12. Sane SP, Dickinson MH. The aerodynamic effects of wing rotation and a revised quasi-steady model of flapping flight. *Journal of Experimental Biology* 2002; **205**:1087–1096.
13. Ellington CP, van den Berg C, Willmott AP. Leading edge vortices in insect flight. *Nature* 1996; **384**:626–630.



DOI: 10.1002/fld

14. Rayner JMV. A vortex theory of animal flight. *Journal of Fluid Mechanics* 1979; **91**:697–763.
15. Vest MS. Unsteady aerodynamic model of flapping wings. *AIAA Journal* 1996; **34**(7):1435–1440.
16. Smith M, Wilkin P, Williams M. The advantages of an unsteady panel method in modeling the aerodynamic forces on rigid flapping wings. *Journal of Experimental Biology* 1996; **199**:1073–1083.
17. Liu H, Ellington CP, Kawachi K. A computational fluid dynamic study of hawkmoth hovering. *Journal of Experimental Biology* 1998; **201**:461–477.
18. Sun M, Tang J. Lift and power requirements of hovering flight in Drosophila virilis. *Journal of Experimental Biology* 2002; **205**:2413–2427.
19. Sun M, Wu JH. Aerodynamic force generation and power requirements in forward flight in a fruit fly with modeled wing motion. *Journal of Experimental Biology* 2003; **206**:3065–3083.
20. Wang ZJ. Two dimensional mechanism for insect hovering. *Physical Review Letters* 2000; **85**:2216–2219.
21. Qun H, Jiang ZL. Measurement of parameters from the beating wings of a bumblebee. *Transactions of Beijing Institute of Technology* 2003; **23**(4):444–448.
22. Van Den Berg C, Ellington CP. The three-dimensional leading-edge vortex of a hovering model hawkmoth. *Philosophical Transactions of the Royal Society of London*, *Series B* 1997; **353**:329–340.
23. Ellington CP. The novel aerodynamics of insect flight: application to micro-air vehicles. *Journal of Experimental Biology* 1999; **202**:3439–3448.



DOI: 10.1002/fld